Danish Meteorological Institute
Ministry of Transport

Scientific Report 05-08

Global Maps from GPS Radio Occulation Data

Siebren de Haan

KNMI, The Netherlands, Siebren.de.Haan@knmi.nl

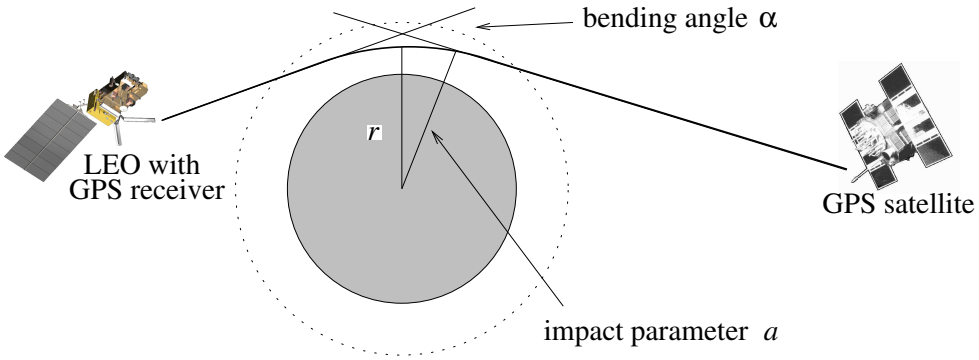

Colophone

Serial title:
Scientific Report 05-08

Title:
Global Maps from GPS Radio Occulation Data

Subtitle:

Authors:
Siebren de Haan
KNMI, The Netherlands, Siebren.de.Haan@knmi.nl

Other Contributers:

Responsible Institution:
Danish Meteorological Institute

Language:
English

Keywords:

Url:
www.dmi.dk/dmi/dmi-publikationer.htm

ISSN:
1399-1949

ISBN:
87-7478-528-1

Version:

Website:
www.dmi.dk

Contents

Global Maps from GPS Radio Occulation Data

Siebren de Haan
KNMI, The Netherlands, Siebren.de.Haan@knmi.nl

1. Introduction

Geopotential heights of constant pressure have become common practice in detecting global warming (Wallace et al. (1993)). The reasoning for the use of this technique lies in the fact that the geopotential height at a constant pressure is directly related to the bulk temperature of the atmosphere from the surface to the pressure level. The common method for determining the geopotential height from observations is based on radiosonde profiles. Because of the restriction to land of these observations, assimilation models are generally used to obtain global maps of geopotential heights. Moreover, there are known problems with certain type of radiosondes due to for example ice contamination of the humidity sensors or day/night inconsistencies (Leiterer et al. (1997) and Lorenc et al. (1996)). Radiosonde observations are also subject to biases and non-systematic errors caused by sensor malfunctions. The quality of a radiosonde observation is also depending on the age of the sensor and proper calibration before launch.

Leroy (1997) presented a new approach for measuring geopotential heights from space. The technique is based on the use of radio occultation technique using the global positioning system (GPS). The advantage of this technique is that all assumptions are known and the distribution of the observations is global. Not unimportant is the fact that the measurement is in essence a time difference and thus inherently self calibrating. This implies that different GPS receivers should be able to deliver data with a common quality.

With the proposed launch of METOP carrying a GPS receiver (called GRAS, Global navigation satellite system Receiver for Atmospheric Sounding) this data will become available for operational use. METOP will be Europe's first operational polar-orbiting weather satellite. When it is launched towards the middle of this decade, it will replace one of two satellite services operated by the United States National Oceanic and Atmospheric Administration (NOAA).

Background of Radio Occultation

The atmospheric data used in this study will be obtained using the technique of Radio Occultation. RO has been an important part of NASA's planetary program since the early 1960's. It has been used to study the atmospheres of Venus, Mars, Jupiter, Saturn and its ring structures, Uranus, Neptune and a number of planetary moons (Fjeldbo et al. (1971), Marouf et al. (1986), Melbourne et al. (1994) and references therein). A short outline of the technique is given below.

In the case of a planetary occultation a radio signal is transmitted from a probe (Mariners in the case of Mars and Venus, Voyager I and II in the case of Jupiter and the other outer planets) through the vertical extent of the planet atmosphere towards the Earth. Here the signal is received, in general with large-dish deep space antennas. The receiver hardware is locked to the radio link as it traverses the planet's atmosphere. The phase-shift that the signal undergoes because it travels through a

medium of varying optical density is measured as a function of the geometrical height of the signal path through the atmosphere. From these phase-shifts vertical profiles of so-called bending angles can be obtained. The bending angle of a ray path is the angle between the physically realized path as determined by the optical medium and the straight line path that would have been taken by the ray if no atmosphere had been present. The bending may take place towards the planet or away from it, depending on the local refractivity gradients (Born and Wolf (1980)). The bending angle profile can be inverted yielding vertical profiles of the atmospheric refractivity. From the (ideal or van der Waals) gas equation and the common assumption of hydrostatic equilibrium of the planet's atmosphere vertical profiles of temperature and density can be obtained (Fjeldbo et al. (1971) in the case of the atmosphere of Venus). In this way the most accurate information pertaining to planetary atmospheres has been obtained.

Planetary atmosphere information has also been obtained using stellar occultation; brightness distributions of extra-galactic radio sources have been studied when occulted by the moon (Melbourne et al. (1994)). RO probing of the atmosphere of Saturn's moon Titan has been useful during the preparation of the Cassini mission.

In the past, mainly because of signal tracking difficulties, space-based RO has never been used for the study of the Earth's atmosphere itself, but this has changed since the successful Proof of Concept project GPS-MET in 1995, a collaboration between UCAR and JPL. For this project a micro-satellite was launched in a 700 km polar orbit with a receiver on board optimized for the two frequencies on which the satellites of the Global Positioning System (GPS) broadcast. This receiver probed the GPS satellites through the Earth' s atmosphere until the moment that they disappeared behind the Earth' s limb. The imprint of the atmosphere on the transmitted signals manifests in a Doppler shift of the signal. A detailed description of how the Doppler shifts of the received signal lead to bending angles is given in Fjeldbo et al. (1971).

The GPS satellites broadcast on two microwave frequencies in order to enable elimination of the effect of the Earth's ionosphere on the received radio signal. The ionosphere, consisting of free electrons, has a rather large variability due to the 11 year solar cycle, seasonal and diurnal variations and the exact transmitter-receiver geometry with respect to the sun's location. By using combinations of two frequencies it is possible to eliminate the ionospheric contribution to the phase-shift of the received signal (Hofmann-Wellenhof et al. (1992))

Vertical temperature profiles with an accuracy of 1 K at the 250 K level (Kursinski et al. (1996)) were obtained, in the absence of water vapor. Because of ambiguity between temperature and humidity in the retrieved atmospheric refractivity some care must be taken in the retrieval process. Temperature profiles can be obtained using ancillary information on the water vapor distribution; humidity profiles can be obtained using additional information on the temperatures. In both cases model data can be used to remove the ambiguity.

Leroy (1997) has investigated the use of the GPS-MET data for the calculation of geopotential heights of constant-pressure surfaces. He used ancillary information on the Earth's gravity field (the so-called JGM-3 model). However in this study only a rather limited amount of data of sufficiently high quality could be used.

Objectives of this study

Long term time series of Global maps of geopotential heights reveal atmospheric (bulk) temperature change. Global (monthly) mean values temperatures are used as parameters to estimate the global warming. In this report an algorithm for creating global mean maps from GPS-RO observations is

investigated.

There are a number of different methods to estimate a global value; all methods need some kind of a priori information. For instance Kriging use time series to predict a value at a certain location and time. Covariances between observations are used as a priori information in Kriging-theory. Another method is (variational) assimilation of observations. This method is widely used in meteorology and is able to combine all kinds of information to estimate the state of the atmosphere at a certain time. Observation error and background error characteristics should be known. Global maps can also be retrieved through simply fitting a set of basis functions to the observations. This method is straightforward when only one type of observation with uncorrelated observations is used. Furthermore, the fitted global map obtained from data from a monthly period is the mean of the observations over a month. Bayesian fitting is an extension of least squares fitting which simultaneously estimates the optimal number of basis functions using a penalty matrix for the coefficients. This method will be used and explained in this report.

Report Outline

In this study the quality of global maps derived from GPS-RO is discussed. First a description of the RO technique is given. The data used in this study is presented also in Chapter 2. Next a technique is described to obtain global fields from GPS-RO data. The retrieval of global maps is based on Bayesian fitting. In Chapter 4 the accuracy of the fitting method is presented, based on real GPS-RO data and simulated data from ECMWF. The latter data source is used to obtain a general idea of the quality of the global maps that will be derived based upon future METOP GRAS data. Chapter 5 is dedicated to the results of the global and zonal fitting. The last chapter contains conclusions.

2. GPS Radio Occultation Data

In this chapter a description is given of the data used in this study. First the method of retrieving atmospheric parameters is described. Next, the coverage and quality of the real CHAMP data, as processed by DMI is discussed. And last, the coverage of simulated METOP observations is discussed in which case the observed atmospheric parameters are obtained using ECMWF analysis fields.

Atmospheric parameters from GPS-RO data

GPS-RO observations are obtained using a GPS receiver on board of a LEO (Low Earth Orbiting) satellite. The observations are the arrival time and frequency of the emitted radio-signal of an occulting GPS satellite (see Fig. 2.1) and thus can be regarded as self-calibrating. The observed

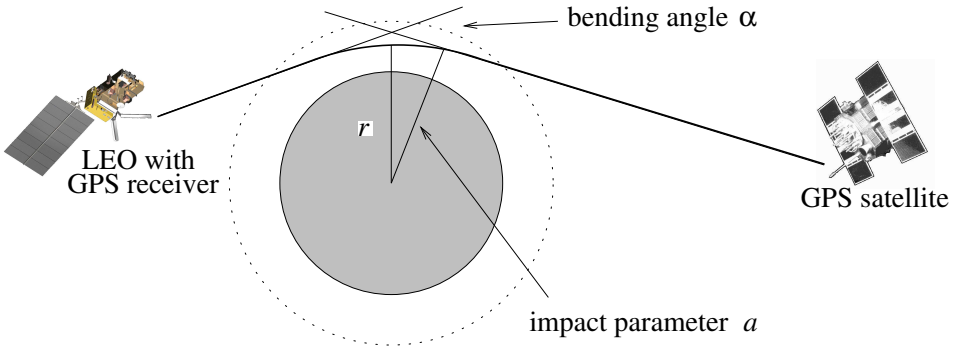

Figure 2.1: GPS-RO geometry.

parameter is bending angle α at a geometric height r. The impact parameter a is defined as

$$a = n \cdot r, \tag{2.1}$$

where n is the refractive index at height r. The relation between bending angle α and impact parameter a is given by the formula of Bouguer

$$\alpha(a) = -2a \int_a^\infty \frac{1}{\sqrt{r^2 n^2 - a^2}} \frac{d\ln(n)}{dr} dr. \tag{2.2}$$

Using Abel inversion the observed bending angle profile can be converted into a refractive index profile. This inversion assumes spherical symmetry. The index of refraction now becomes

$$n(a) = \exp\left(\frac{1}{\pi} \int_a^\infty \frac{\alpha(x)}{\sqrt{x^2 - a^2}}\, dx\right). \tag{2.3}$$

The ellipsoidal height h is determined as

$$h = \frac{a}{n} - R_{curve}, \tag{2.4}$$

with R_{curve} is the radius of curvature at the tangent point. The singularity in Equation (2.3) is solved by a change of variables (i.e. $x = a\cosh(\theta)$) and assuming that the bending angle is an exponential function in between measured values.

Above a height of approximately 50 to 60km the bending angle observation drops below the thermal noise in the receiver. Because of the infinity in Equation (2.3) an assumption has to be made for the bending angle values at high altitudes. Two possible methods are available to tackle this problem: extrapolating α with an (exponential) function or use information from a neutral model. The latter method is used in this study; the neutral model is MSIS90 (see Hedin (1991)). This method is a statistical optimization of the bending angle (Rodgers (1976)) using the statistical method proposed by Hocke et al. (1997). The receiver signal noise is reduced by a low-pass filter. More detailed information can be found in Rubek (2004).

The refractivity N has contributions from four main sources at microwave lengths: dry or neutral atmosphere, water vapour, free electrons and (primarily) liquid water. The contributions of the free electrons can be eliminated by a linear quotient of the calculated bending angles representative obtained at two frequencies. The scattering due to liquid water droplets is small compared to the other terms and is therefore omitted (Kursinski et al. (1997)). The dry refractivity is proportional to the number density and is dominant below the ionosphere. The wet refractivity is primarily due to the large dipole moment of water vapour and is most pronounced in the lower part of the troposphere. The refractive index and refractivity are defined as (Bevis et al. (1992))

$$\begin{aligned} N &= \left(k_1 \frac{p}{T} + k_2 \frac{e}{T} + k_3 \frac{e}{T^2}\right). \\ &= (n-1)10^6, \end{aligned} \tag{2.5}$$

where $k_1 = 77.6K/hPa$, $k_2 = 70.4K/hPa$ and $k_3 = 3.739 \cdot 10^5 K^2/hPa$ are constants (Bevis et al. (1992)).

The geopotential height is calculated from geometric heights using the gradient of the gravitation potential with height and the mean gravity values on the geoid based on the gravity model EGM96

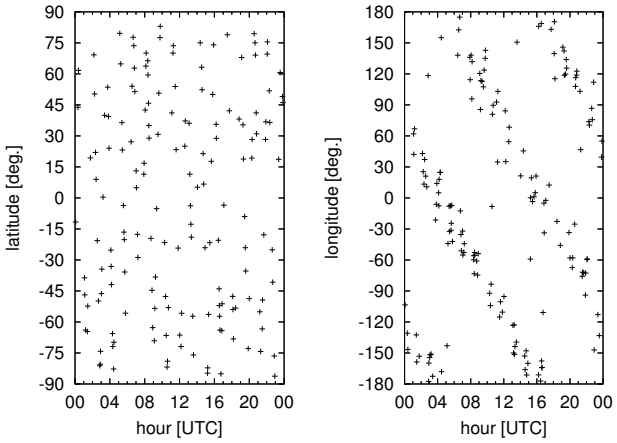

Figure 2.2: Coverage of CHAMP RO data for a single day.

(Lemoine et al. (1998)). The dry pressure at a certain height is calculated from Equation (2.5) and the dry ideal gas law together with the equation of hydrostatic equilibrium by

$$P_{dry}(h) = \int_h^\infty \frac{N}{k_1 R_d} g dh, \tag{2.6}$$

where g is the gravitational potential as a function of height and R_d is the universal gas constant of dry air. Because of the infinity upper limit of the integral, assumptions on the upper limit has to be made.

CHAMP data

The real data used in this study stems from the research satellite CHAMP (Wickert et al. (2001)). The orbit height of the satellite was in 2003 approximately 300km and it is decreasing gradually. The global coverage of one day of data is shown in Figure 2.2. Time of day is on the horizontal axis and longitude and latitude are on the vertical axis for the left and the right plane respectively. Clearly visible is the band-wise behaviour in the longitude direction while the latitude shows a more randomly spreading of the data. CHAMP data does not sample the global diurnal in a random matter. The fact that CHAMP scans in longitude bands results in observations obtained at the same times during different days. In Figure 2.3 the coverage of CHAMP data around 12 UTC is shown for observations from one month. Again, clearly visible is the fact that the locations are in bands and thus certain longitude bands are not observed during one month at 12 UTC.

Quality Control

For a period of 18 months CHAMP data has been processed by DMI. All data needs a quality control preferably not relying on external data sources because this data source may also be subject to errors. For CHAMP data, an easy check would have been to compare it to ECMWF observations. However, especially in regions where CHAMP observes (over oceans in the southern hemisphere) the ECMWF is not necessarily correct (Gobiet et al. (2005)). Therefore requirements for a profile to pass quality control are based purely on profile data itself and kept as close as possible to the observation (i.e. refractivity). It turned out that there was a need to include also temperature in the quality, although this is not a directly observed parameter its physical boundaries are well known. A quality control was performed on the profiles with the following requirements

- Data present between 40 to 60km.

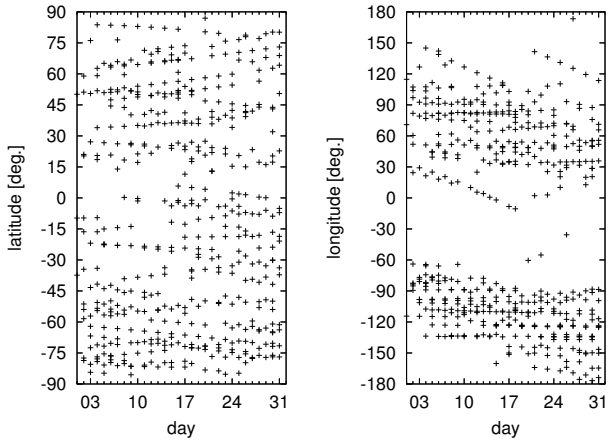

Figure 2.3: Coverage of CHAMP RO data around 12 UTC for one month.

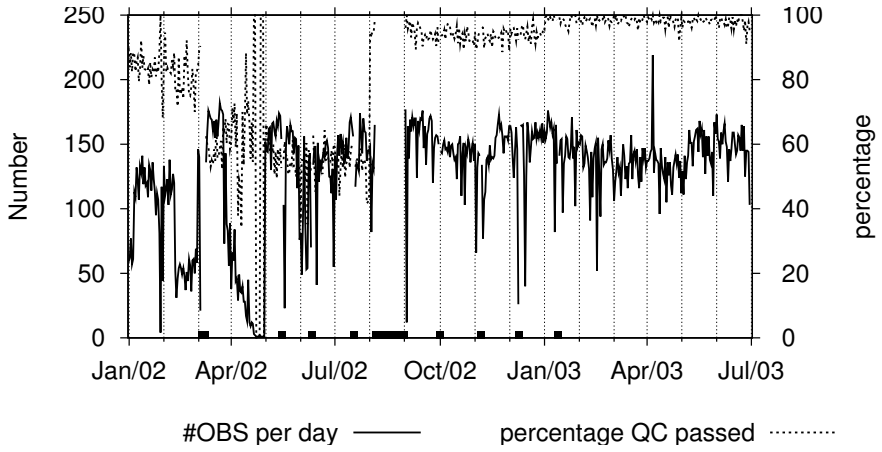

Figure 2.4: Amount and Quality of CHAMP data for a 18 month data set.

- Refractivity N larger than 0
- For $40 < z < 60$km : Max $dT/dz < 10$K/km and $\sigma(dT/dz) < 5$K/km
- For $50 < z < 60$km : T-range < 50 K
- dT/dz should not change sign suddenly

In Figure 2.4 the number of observations and percentage of good observations per day are shown. From Figure 2.4 one can see that there are roughly two periods; one before September 2002 and one after September 2002. Before September 2002 the number of data points were highly fluctuating and the percentage of "good" observations was also not stable. After September 2002 the number of observations is more or less stable and also the percentage of "good" data is more or less stable albeit that there is a small jump from around 90% to 95% around January 2003. Later in this study we focus on the data set from January to July 2003.

Simulated METOP data

The METOP satellite will be launched in 2006. To give an impression on the data coverage of the GPS-RO data from this satellite a simulation of the orbits (both GPS satellites and METOP) was performed. In Figure 2.5 the coverage is shown for one day. Again a band-wise pattern is visible, although the distribution is a little less within stringent bands than CHAMP data is. The difference

between CHAMP and METOP in this sense is primarily related to the difference in satellite orbit (METOP 800km and CHAMP 300km). When the locations of METOP observations from around 12 UTC are plotted for a one month period a different pattern is observed than for CHAMP data. All longitudes are observed, albeit that there are two regions which have a higher density in observations, see Figure 2.6.

3. Estimating Global Maps

Introduction

There are several ways of obtaining global maps from a data set of observations. When one wants stay as close as possible to the observations Kriging or simply fitting are good candidates. Both methods have disadvantages. Fitting assumes that the data set can be expressed by a (finite) set of basis functions. For the Kriging method observation correlations are needed. Moreover, the resulting global map will have a different physical meaning, that is, it will be a estimate of the parameter at a certain time, while fitting a single global map from a (long) time series data set results in a mean value over the time window. Because our focus is here on global mean maps, fitting data sets is used here.

Fitting a data of set (x_i, y_i) of N points is equal to minimizing the distance between this data set and

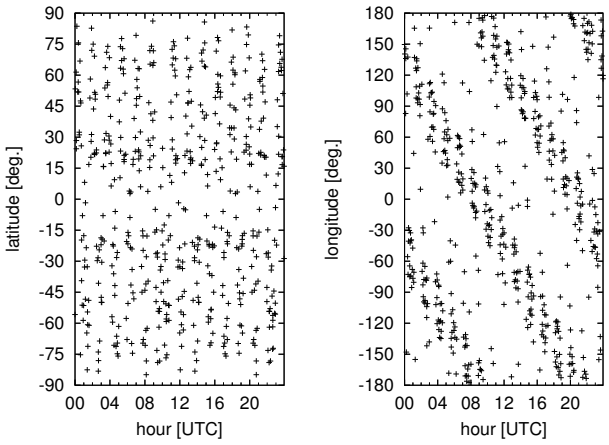

Figure 2.5: Coverage of METOP RO data for a single day

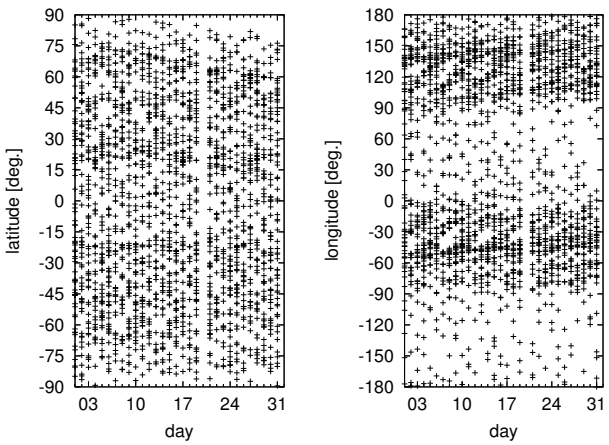

Figure 2.6: Coverage of METOP RO data at 12 UTC for one month period.

a certain function. Here x is the location and y can be the geopotential height. The fit is defined as

$$y(x) = \sum_{k=1}^{M} w_k \phi_k(x), \tag{3.1}$$

where $\phi_k(x)$ is basis function k (in this report spherical harmonics are used, $k = (l, m)$ degree l and order m, see Appendix A). Finding the best fit is reduced to finding the values w_k for which the fit is optimal. The definition of 'optimal' creates different method of fitting data. Furthermore, the number of basis functions will influence also the 'optimality' of the fit.

Least χ-squared Fit

Most algorithms are based upon the least χ-squared fit. A set of basis functions is chosen and the coefficients w are determined such that the following sum is minimized:

$$\chi^2(w) = \sum_{i=1}^{N} \left(\frac{y_i - \sum_{k=1}^{M} w_k \phi_k(x_i)}{\sigma_i} \right)^2, \tag{3.2}$$

where σ_i is the uncertainty of each measurement. Define a $(M \times N)$-matrix Φ as

$$\Phi = \{\phi_k(x_i)\sigma_i^{-1}\} \tag{3.3}$$

and N-vector y as

$$y = \{y_i \sigma_i^{-1}\}, \tag{3.4}$$

the minimization can be rewritten as

$$\min_w (y - \Phi w)^T (y - \Phi w) \tag{3.5}$$

The optimal value of w in the least χ-squared sense can be found by finding w such that the derivative of Equation (3.5) with respect to w is zero, that is

$$w = B^{-1} \Phi^T y, \tag{3.6}$$

where the matrix B is defined as

$$B = \Phi^T \Phi. \tag{3.7}$$

Note that when all measurements have the same uncertainty σ the solution given by Equation (3.6) is independent of σ. An estimate of the standard deviation for the coefficients w is calculated using the derivative of w_j to y_i

$$\sigma^2(w_j) = \sum_{i}^{N} \sigma_i^2 (\frac{\partial w_j}{\partial y_i})^2 \tag{3.8}$$

From Equation (3.6) the derivative to y_i is

$$\frac{\partial w_j}{\partial y_i} = \sum_{k=1}^{M} B_{jk}^{-1} \, \phi_k(x_i)/\sigma_i^2. \tag{3.9}$$

This gives the following expression for the standard deviation of coefficient w_j

$$\sigma^2(w_j) = B_{jj}^{-1}. \tag{3.10}$$

Bayesian Fit

Bayesian Fit is a method to find the best fit of a function to a data set based on a cost function. Fitting data involves a number of assumptions; first the type of basis function is selected, secondly the number of basis functions to use is chosen. Setting the number of free parameters w equal to the number of data points N will most likely result in an over fit of the data. A too small number of basis functions will lead to under-fitting: the best choice lies in between. The prior information needed for to find the best choice is a given regularizing function closely related to a penalty function. The cost function is defined using bayesian theory and the solution maximizes the evidence (with respect to the number of basis functions) and minimizes the cost function (with respect to the data and the number of basis functions).

The algorithm is an advanced least χ squared minimization; the result is a most probable fit with a error estimated of the fit. The least χ squared fit problem definition is expanded with a penalty matrix C. Now the minimization problem becomes: find a minimum for $M(w, \alpha, \beta)$ where

$$\begin{aligned} M &= \beta E_d + \alpha E_w, \\ E_d &= \frac{1}{2}(y - \Phi w)^T (y - \Phi w), \text{ and} \\ E_w &= \frac{1}{2} w^T C w. \end{aligned} \tag{3.11}$$

The parameter β is related to the uncertainty in the observations and α can be regarded as a measure of how smooth the fit is expected to be. Note that when α is set to zero, the above equation define a normal least χ-square fit problem with a uncertainty in the observations of $\sigma^2 = 1/\beta$. The definition of y and Φ differ slightly from the definition given in the previous section, that is

$$\Phi = \{\phi_k(x_i)\} \text{ and } y = \{y_i\}. \tag{3.12}$$

MacKay (1992) describes a method to compare different models (e.g. different number of spherical harmonics) and to select the optimal choice by maximizing the evidence of a model. The evidence of a model is defined as the probability of a certain choice of w given the data set $D = (x_i, y_i)$, the basis functions ϕ_k and a prior with regularizer R. The latter describes the smoothness of the fit (defined in the above by E_w). Using Bayes' rule, the posterior probability is defined as

$$\begin{aligned} P(w|D, \alpha, \beta, \phi, R) &= \frac{\text{Likelihood} \times \text{Prior}}{\text{Evidence}} \\ &= \frac{P(D|w, \beta, \phi) P(w|\alpha, \phi, R)}{P(D|\alpha, \beta, \phi, R)}. \end{aligned} \tag{3.13}$$

The "Evidence" (abbreviated as E) is commonly ignored because it is purely related to the choice of type and number of basis functions ϕ. However, the evidence E turns out to be useful when comparing different fitting procedures as will be explained below. The observed data points can be modeled as a the fitted value with a noise term, that is

$$y_i = y(x_i) + \epsilon_i. \tag{3.14}$$

Suppose that ϵ_i can be modeled as a zero-mean Gaussian with a standard deviation of σ_ϵ then the probability of the data given the parameters w is

$$P(D|w, \beta, \phi) = \frac{\exp(-\beta E_D)}{Z_D(\beta)}, \tag{3.15}$$

where $\beta = 1/\sigma_\epsilon^2$, $Z_D(\beta) = \int d^k(x_i, y_i) \exp(-E_D) = (2\pi/\beta)^{N/2}$ (See MacKay (1992) for more details). Following MacKay (1992) the prior and the posterior can be modeled as

$$P(w|\alpha, \phi, R) = \frac{\exp(-\beta E_W)}{Z_D(\alpha)}, \tag{3.16}$$

$$P(w|D, \alpha, \beta, \phi, R) = \frac{\exp(-M)}{Z_M(\alpha, \beta)} \tag{3.17}$$

where $Z_W(\alpha) = \int d^k w \exp(-\alpha E_W)$ and $Z_M(\alpha, \beta) = \int d^k w \exp(-M)$. The Evidence now becomes, using $M = \beta E_d + \alpha E_w$,

$$P(D|\alpha, \beta, \phi, R) = \frac{Z_M(\alpha, \beta)}{Z_W(\alpha) Z_D(\beta)} \tag{3.18}$$

Assuming that R is a quadratic functional (which is the case here, see Eq. 3.11) then Z_M becomes a Gaussian integral:

$$Z_M = e^{-M(w_{mp})} (2\pi)^{k/2} \det^{-1/2} A, \tag{3.19}$$

where $A = \nabla\nabla M = \beta \Phi^T \Phi + \alpha C$ and w_{mp} is the solution of Equation (3.11) given by

$$w_{mp} = A^{-1} \beta \Phi^T y \tag{3.20}$$

and logarithmic of the evidence of the model can be written as

$$\begin{aligned} \log(E) \quad = \quad & -\alpha E_w(w_{mp}) - \beta E_d(w_{mp}) \\ & -\frac{1}{2} \log\det A + \frac{1}{2} M \log\alpha + \frac{1}{2} N \log\beta - \frac{1}{2} N \log 2\pi \end{aligned} \tag{3.21}$$

An estimate of the standard deviation in the w is obtained in a similar way as for the least χ squared fit:

$$\sigma^2(w_j) = \sum_{i=1}^{N} \sigma_\epsilon^2 \left(\frac{\partial w_j}{\partial y_i} \right)^2 = \beta((A^{-1})^T A^{-1} \Phi^T \Phi)_{jj} \tag{3.22}$$

(see Appendix B for more details.)

The Bayesian fitting method has three levels of inference. The first level is finding the most probable solution w_{mp}; next find α and β that minimize M; and then determine the evidence (see also Appendix C). Using the evidence different models can be compared which is the last level of inference. The model with the largest eveidence can be considered as the best one to choose.

Measuring the Distribution of Global Data

At a first approximation, the earth surface can be regarded as a sphere. Because the goodness to fit a data set globally is related to the distribution of the data over the earth surface, some insight in optimal spherical distributions is useful here. In normal rectangular plane, a Gaussian distributed data set is easily constructed. For spherical surfaces, this is not straight forward. Here we use the algorithm as developed by Galassi et al. (2003). In Figure 3.1 880 points are plotted randomly over the earth surface. To evaluate whether or not the observations are well distributed the following method is developed. The earth surface is partitioned in L area's in the following way. First, L points are distributed over the earth surface such that distances over the earth surface between neighboring points are more or less equal. These L points define regions with equal areas as can be seen in Figure 3.2 (with $L = 40$); the relative area size is plotted in Figure 3.3 by the dashed line. By

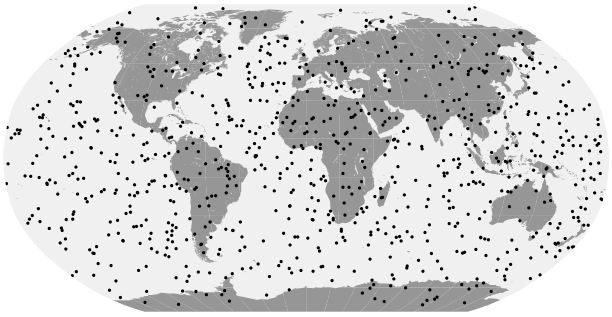

Figure 3.1: Randomly distribution of 880 points over the globe.

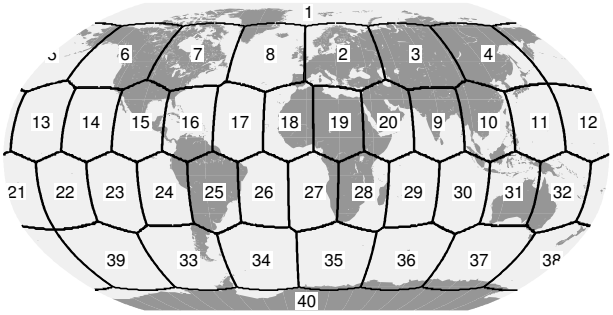

Figure 3.2: Partitioning of the earth surface in 40 (almost) equal area's.

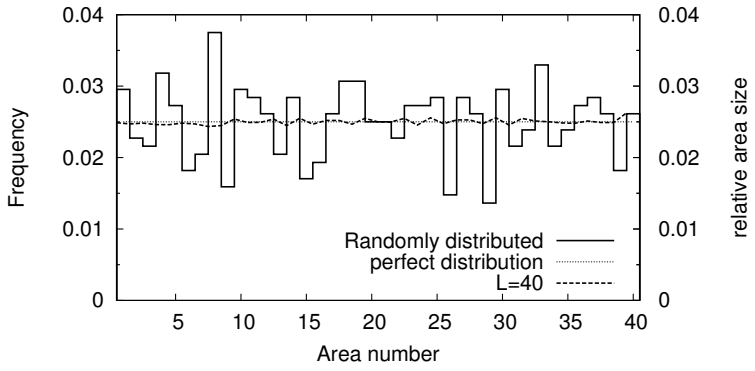

Figure 3.3: Frequency of randomly distribution of 880 points (solid line); the perfect distribution is represented by the dotted line and the (relative) area size is denoted by the dashed line.

counting the number of observations per area, an estimate of the distribution can be obtained. In Figure 3.3 these statistics are shown for the randomly distributed points shown in Figure 3.1. As expected, the number of points are nearly equal for all area's. The dotted line represents the perfect distribution, and the deviation from this line is caused by the randomness of the points. Note also that the (relative) area size is almost equal 1/40 for all area's as can be seen from this figure by the dashed line.

4. Accuracy Estimation of Bayesian Fit

In this chapter the theoretical definition of the the accuracy of the fit coefficients are explored with some numerical examples. First some remarks are made concerning the horizontal resolution of a field represented by spherical harmonics. Next the quality bayesian fitting is discussed using simulated observations. Hereafter the optimal number of spherical harmonics is determined for different geopotential heights, different observation windows and different satellites (i.e CHAMP

and METOP).

Resolution

Laprise (1992) discussed that there is not a general definition of horizontal resolution related to spherical harmonics. Resolutions defined by different methods may differ by 20%. A widely used notion of resolution is defined by the number of coefficients defining the equator

$$L_{SH} = \frac{2\pi R_E}{2M+1}, \tag{4.1}$$

where R_E is the earth radius and M is the number of spherical harmonics. For the current operational ECMWF model ($M = 511$) this implies that $L_{SH} \approx 39km$.

Suppose that we have K perfectly distributed observations. The mean area for which an observation is representative can be written as

$$L^2 = \frac{4\pi R_E^2}{K} \tag{4.2}$$

Suppose now that the observations are Gaussian distributed over the earth surface. Because of the probability that there are areas with no observations an over sampling seems to be appropriate. Here an over sampling of 4 is chose (2 in both directions) which results in a resolution of

$$L_{OBS} = 4\sqrt{\frac{\pi}{K}} R_E \tag{4.3}$$

Combining this with the estimated resolution of a spherical harmonics fit we obtain the following relation

$$M = \frac{1}{4}\sqrt{\pi K} - \frac{1}{2} \tag{4.4}$$

Although GPS-RO data has a global coverage, the number will not be large enough for a fit with high horizontal resolution. The daily number of CHAMP observations is approximately 200 and thus the minimal resolution is $L = 3080km$. Based on daily data a fit with maximal 6 spherical harmonics can be constructed. When one month of data is used the maximal number of spherical harmonics is 36 ($L = 550km$), however this value will never be reached because of the variability of the atmosphere (within one month) and uncertainties in the observations. METOP will have approximately 500 observations per day which implies $M = 9$ and $L = 2110km$, while monthly fits will maximal have $M = 51$ and $L = 390km$.

Penalty matrix for Bayesian Fitting

The bayesian method of fitting requires a penalty matrix. Leroy (1997) proposed a matrix such that the global mean must be weighted less than the others and purely meridional terms must be weighted less than the rest. Here a more simple penalty matrix is introduced: matrix C is defined as

$$C_5 = (m+1)^5, \text{ for } m = 0..M \tag{4.5}$$

The reason for this choice is: higher frequencies in longitude are penalized, the factor 5 is chosen such that the estimated standard deviation of the geopotential height and the standard deviation from monthly ECMWF fields are simular; this will be discussed in Section 4.4.1. The bayesian fitting procedure determines 'best fit' and the optimal number of spherical harmonics simultaneously.

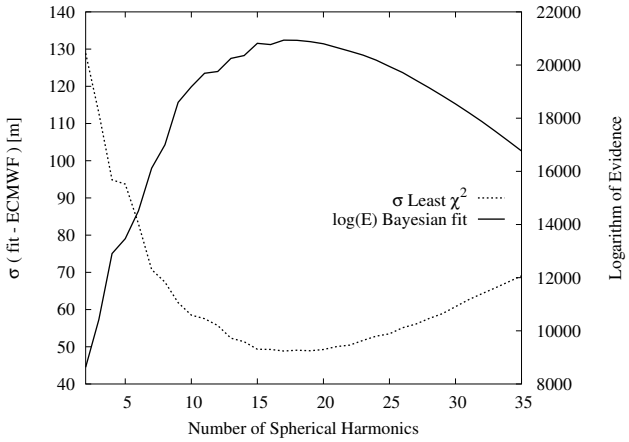

Figure 4.1: Result of bayesian fit for one day (17 May 2003) with simulated observations. The number and coverage of the observations can be compared to one month of METOP observations

The Optimal Fit

Generally, the truth is unknown and thus a correct estimate of the fit can not be measured. To obtain some insight in the quality of the fit, ECMWF analysis fields are used as the truth and observations are deduced from these fields. Next these observations are used to derive the optimal fit in bayesian terms which then can be compared to the original ECMWF field.

Using Perfect Observations

The ECMWF analysis valid for 17 May 2003 at 1200 UTC is used to derive observations at (simulated) METOP locations for a complete month. The observed parameter is the 500hPa geopotential height. The number of observations is 14809 which results in maximal $M = 53$ according to Equation (4.4). This is a very optimistic estimate because the coverage will not be a Gaussian distributed but will have a repetitive cycle because both METOP and the GPS satellites are in circular orbits (see Figures 2.5 and 2.6).

In Figure 4.1 the logarithm of the evidence is shown together with the standard deviation of the fit with the truth. There appears to be a optimal value $M = 17$ for which the evidence attains a maximum. For this value of M the standard deviation with the truth is also minimal. For larger M the evidence decreases due to the increase in spherical harmonics coefficients. The standard deviation with the truth increases due to over fitting the data set. The bayesian method also estimates the uncertainty of the data with respect to the fit ($\beta^{-1/2}$). In Figure 4.2 again the standard deviation between the fit and the truth is shown together with the estimated fit accuracy. The accuracy of the fit decreases with increasing M which is due to the fact that the fit will match the data set better when more harmonics are used. Furthermore, the estimated accuracy lies close to the standard deviation with the truth for all M smaller than the optimal value $M = 17$. When over fitting occurs the standard deviation and estimated accuracy diverge. From these two figures we may conclude that the optimal M is 17 and that the accuracy of the fit is approximately $50m$.

The data used in the previous fitting experiment was derived from an analysis field valid at a specific time. A more realistic data set is obtained by deriving observations from one month of ECMWF analysis. These analysis are obtained every 6 hours. In this way the atmospheric variability is simulated. When fitting this data set an estimate of the monthly mean is determined based on the observations. Note again that the observations are prefect, in the sense that there is no observation noise. The truth is now the mean of the monthly ECMWF analysis. In Figure 4.3 the evidence of the

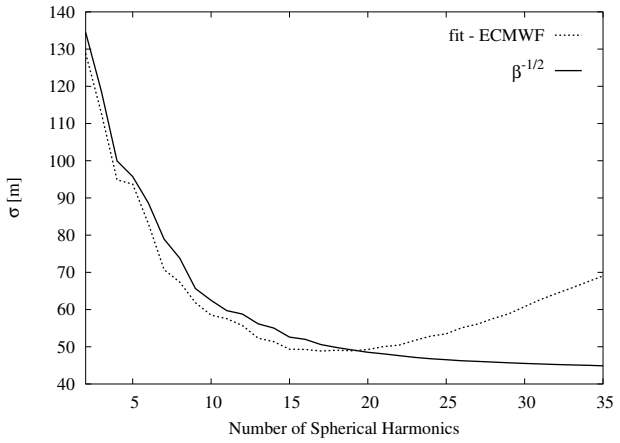

Figure 4.2: Analogous to Fig. 4.1; visualizing the actual standard deviation of the fit with the truth and estimated accuracy obtained from bayesian fitting.

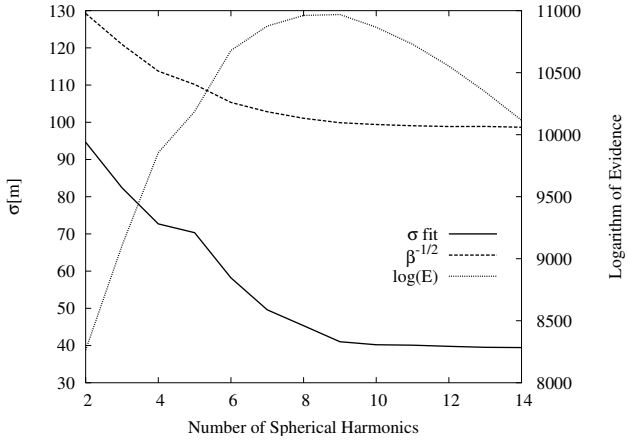

Figure 4.3: Result of bayesian fit for the month 2003/04

bayesian fit is shown together with the standard deviation with the ECMWF monthly mean geopotential height at 500hPa. The data is derived from ECMWF at simulated METOP locations, while the reference field is the mean of geopotential height at 500 hPa. The number of observations is 13249. The optimal value of spherical harmonics is 9. The estimated observation error is also shown in Figure 4.3. The fact that the estimated observation error is approximately $60m$ larger is the due to the fact that now the observations are more realistic, that is, these observations contain information of the normal atmospheric variability during one month. Note also that although the number of spherical harmonics is smaller (here $M = 9$) than in the previous example ($M = 17$), the standard deviation of the fit with the truth is smaller. Monthly averages are smoother than analysis valid at a specific time.

To gain some insight in the dependence of the optimal spherical harmonics fit on the size of the data set two types of data sets are constructed both based on ECMWF analysis valid at one specific time. The first type of data set is based on Gaussian distributed observations over the entire globe. The number of observations varies between 1000 and 12000. The second data set is similar to the data set used in the first example: the observations are derived at (simulated) METOP locations; different data sets are constructed using coverage from different days but with the same ECMWF analysis. In Figure 4.4 the optimal number of spherical harmonics is shown for these two data sets. Clearly visible is the influence of the distribution over the globe of the observations: METOP has a lower optimal number of spherical harmonics than Gaussian distributed data. Also shown in this figure is

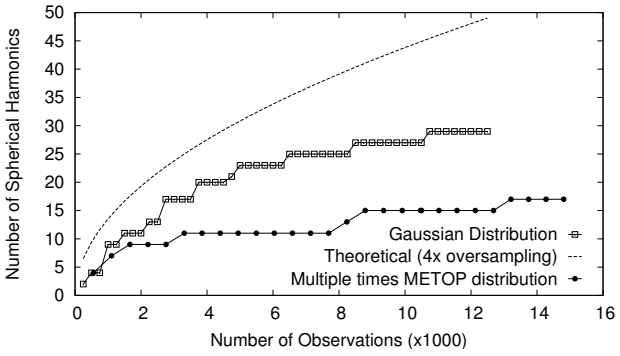

Figure 4.4: Optimal number of spherical harmonics for a perfect Gaussian distribution and a METOP distribution together with the theoretical optimal M.

the theoretical value of optimal spherical harmonics (according to Eq. 4.4): the theoretical value is clearly an upperbound.

Real data

The data used above is derived from ECMWF analysis fields and thus contains no observation error. In this section the influence of observation errors (and coverage) is discussed. The observations used here are obtained from the CHAMP satellite (Wickert et al. (2001)) and are processed by DMI (see Rubek (2004) and Chapter 2). The number and quality of these observations is discussed in Section 2.2.

The influence of the observation error is determined by comparing the results of the fit of real CHAMP data and ECMWF derived CHAMP data at the same locations. Because the lowest observation point of a GPS-RO profile differs from profile to profile, geopotential height at two different pressure levels are used to quantify this difference. One week and one month of observations are fitted to investigate the influence on the data set length.

The result is shown in Figure 4.5. The top left panel shows the optimal number of spherical harmonics using real CHAMP data, the top center panel shows the optimal fit using simulated CHAMP data and for the top right panel simulated METOP observations are used. The optimal fit is determined for the first six months in 2003. No METOP estimate were generated in January 2003. The number of observations used for finding the optimal fit is displayed in the middle panels. Obviously, the middle center panel and the middle left panel show the same amounts of data points used. Note that the number of observations for METOP is approximately three times larger than the number for CHAMP. The bottom panels show the estimated observation error with respect to the fit; this parameter can be regarded as an estimate of the accuracy of the fit.

Optimal fits for weekly data sets are denoted by boxes; the dots are related to the monthly data sets. Geopotential heights at different pressure heights are denoted by different line styles: geopotential height at 100hPa is denoted by a solid line, while the dashed line represents the optimal fit of 500hPa. In general for CHAMP (real or perfect) data, the optimal fit of monthly data has a higher number of spherical harmonics than weekly data. Although the spread around a mean value for monthly data sets is larger than for weekly data sets, the optimal fit M is generally higher. Note that for May the optimal fit of weekly 100hPa data is one spherical harmonic higher than the monthly data set. We may conclude that the number of data points and coverage is important.

Comparing the top left and the top center panel gives an estimate of the influence of the observation

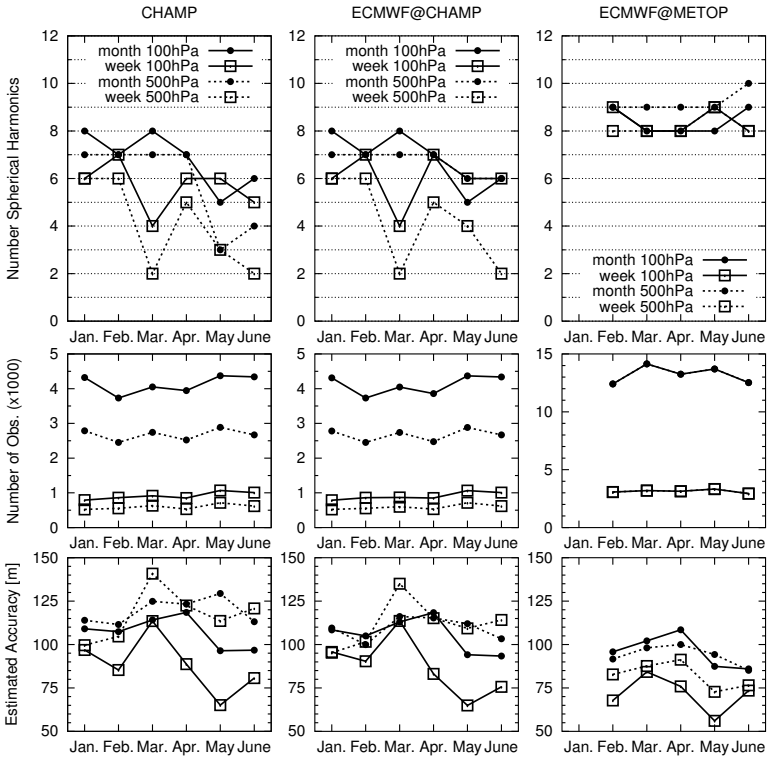

Figure 4.5: Top panels: optimal M for an identity penalty matrix; middle panels: number of observations used for fitting; bottom panels: estimated accuracy ($\beta^{-1/2}$). Data source used are CHAMP, simulated CHAMP and simulated METOP from left to right.

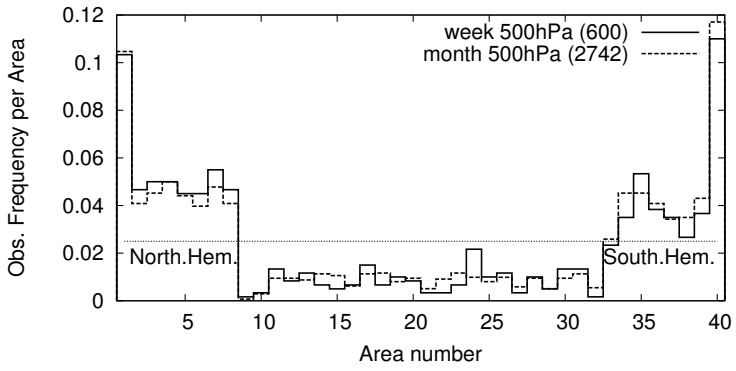

Figure 4.6: Observations distribution of 500hPa CHAMP observations of one week (solid) and one month (dashed) from March 2003.

noise. In general the optimal fit based on "perfect" (ECMWF@CHAMP) data is equal (and sometimes higher) to the optimal fit based on real data. For March 2003 both perfect and real fit show a low optimal number (2) for weekly fits of 500hPa. The estimated accuracy also increases drastically (which is a bad sign). To check whether the distribution of observations is of influence, the frequency of observations per surface area is determined following the method described in Section 3.4. The distribution of the 40 area's is shown in Figure 3.2; the resulting distribution per area is shown in Figure 4.6. From this figure we see that the weekly and monthly distribution are nearly the same, and therefore the observation distribution is not the cause of the difference in optimal M. The distribution of CHAMP data is far from perfect. The equatorial region (area's number 9 to 32) are under sampled by CHAMP. This distribution is general for CHAMP data. The cause of the small number of spherical harmonics may lie in the atmospheric variability in the month

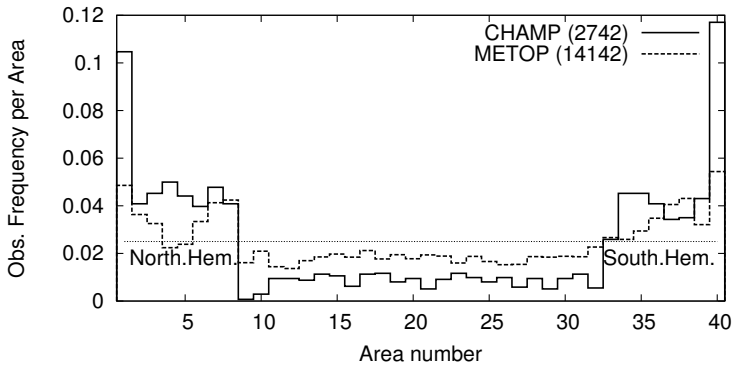

Figure 4.7: Global distribution of CHAMP (solid) and METOP (dashed) observations for one month (2003/03) at 500hPa.

March.

The estimated accuracy value is a good indicator of the quality of the fit. When this value is large compared to other values obtained with similar time windows and parameters, the fit is poor.

Fitting (simulated) METOP data results in a optimal of 9 spherical harmonics. In general this number is higher than the optimal fit by (simulated) CHAMP data. This is not surprising because the number of data points is three times more for METOP. The fact that the optimal number is not higher than 9 is related to the daily variance in the observed geopotential height (see Figure 4.4). Note also that the number of weekly observations is equal for both pressure heights because the observations are derived from ECMWF analysis.

When comparing the distributions of CHAMP and METOP, it is clear that not only the number of observations are of influence on the quality of the global map, see Figure 4.7 The METOP distribution is better in all regions: more observations in the equatorial region and less in the polar regions.

When comparing the estimated accuracy between simulated CHAMP and METOP fits we see that for all four different fits the accuracy of METOP is better and that the difference from month to month is more smooth for all four different data sets.

Performance of the Error Estimate

In this section some insight on the usefulness of the theoretical standard deviation give by Equation (3.22) is obtained. This theoretical standard deviation depends on the choice of penalty matrix C. First the error estimate of the coefficients is investigated; next the error estimate of a fit is quantified.

Coefficient Error Estimate

The mean and standard deviation of the spectral harmonics coefficients of the ECMWF (6 hour analysis) 500hPa geopotential height were determined for the month May 2003. METOP observation location were simulated using the current GPS constellation of 24 satellites and the proposed METOP orbit. Using these locations, for the same month the fit of simulated METOP observations. These observations were subsequently used to estimate the fit; simultaneously an estimate of the standard deviation was obtained. In Figure 4.8 the result of the fit is shown for penalty matrix C_5 together with the observed standard deviation from ECMWF

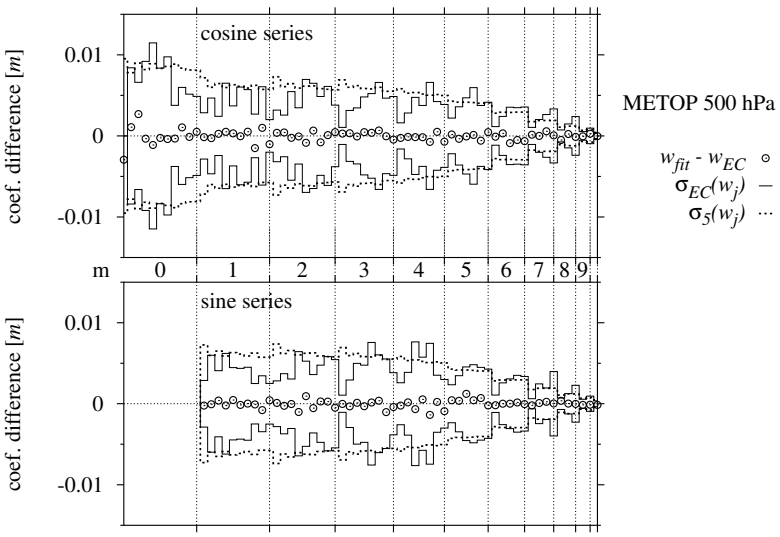

Figure 4.8: Difference between mean of ECMWF spectral coefficients (w_{EC}) and fit. The dashed line is the estimate of the uncertainty in fit coefficients; the solid line is the standard deviation of the coefficients from ECWMF.

Clearly visible is the fact that the standard deviation becomes small for increasing harmonics. The definition chosen here is such that it the penalty becomes larger for increasing harmonics (by penalizing higher harmonics) resulting in a decrease of estimated standard deviation. Also shown in this figure are the differences between the estimated coefficients and the mean of the ECMWF fields. The deviation of the first (i.e mean field value) is large compared to the other values. This is caused by the fact that the distribution in the latitude of the observation location is not perfect.

Fit Error Estimate

The parameter β is related to the "misfit" of the observations relative to the fit. The inverse of the square root of β can be compared to the atmospheric variability of a certain parameter with respect to the mean value of this parameter over a certain period. The number of spherical harmonics determines the amount of misfit. When no atmospheric variability is present the standard deviation with the mean (which is equal to the field itself) is small and thus the fit will also be good. In reality atmospheric variability is present and, although it is not an observation error, when constructing mean global maps over a large time period this variability can be regarded as an extra observation error. In Figure 4.9 the estimated accuracy ($\beta^{-1/2}$) based on observations from CHAMP, simulated CHAMP and (simulated) METOP for May 2003 are shown with respect to the number of spherical harmonics. Also shown in this figure is the standard deviation of the difference of the mean ECMWF field for different values of truncation of spherical harmonics.

The estimated accuracy of CHAMP data consists of an observation error besides the atmospheric variability. By inspection of the difference between the CHAMP fit and the fit using simulated CHAMP data this error can be quantified being approximately 10m. One caution should be made here: all estimated errors are related to number of spherical harmonics used for the fit. The estimated accuracy first decays with increasing harmonics because the data is fitted better by a larger number of harmonics. When the number of harmonics is larger than optimal the estimated error may increase again due to over fitting. The fit based on METOP data decreases and attains a limit.

The change in standard deviation over one month of truncated ECMWF fields is denoted by a solid line and plusses. The standard deviation is increasing because when fields with only a small number

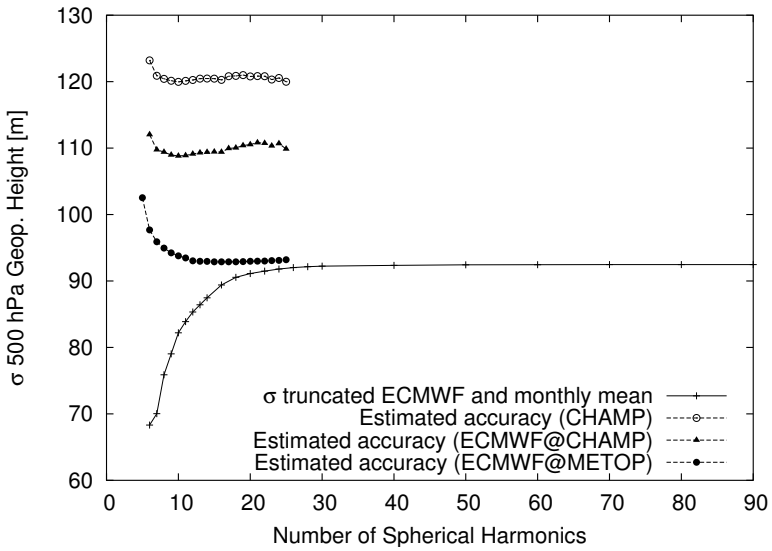

Figure 4.9: Monthly estimated fit error ($\beta^{-1/2}$) and monthly atmospheric variability of ECMWF analysis for the month May 2005. Estimated error is based on observation from CHAMP (dashed line, open circle), simulated CHAMP (dashed line; solid circle) and METOP (dashed line; closed triangle); ECMWF truncated atmospheric variablity versus monthly mean is denoted by a solid line with plusses.

of spherical harmonics are considered small scale atmospheric variability can not be present. Figure 4.9 shows that for fields with more than 30 spherical harmonics the atmospheric variability at 500hPa is more or less constant; the monthly mean of 500hPa geopotential height is well represented by 30 harmonics. The atmospheric variability of 30 harmonics and higher are not visible in the standard deviation with monthly means. The METOP fit attains this value from which we may conclude that METOP data can be used to estimate mean global fields. The fact that (simulated) CHAMP data does not reach the same accuracy as METOP is related to the fact that the number of observation of CHAMP is smaller and the coverage is less optimal compared to the coverage of METOP.

To assess the quality of the fit procedure further a jackknife experiment is conducted. From a 14 day (simulated) METOP data set (2003/05/01 - 2003/05/14) arbitrarily 5 days were excluded to obtain 2002 different data sets. Here a zonal fit is used for presentation purposes. These data sets were then used as observations to find the optimal bayesian zonal fit; the chosen parameter is the refractivity at a certain geometric height. The estimated error in the fit is shown in Figure 4.10 by the grey lines. This figure shows an estimate of the fit accuracy of the refractivity at 10km. Also shown in this figure is the standard deviation of the 2002 fit results (dotted) and the standard deviation of zonal mean values over the same period obtained by excluding arbitrarily 5 days from 14 days (dashed). From this figure we see that the estimated accuracy is an upper limit of of the expected variance due to fitting different data sets. The variance of the 2002 fit is almost equal to the variance in the 2002 different ECMWF fields.

In Figure 4.11 the result of a similar experiment is shown except now for refractivity at a height of 20km. Again the variance of the 2002 fits is similar it the variance of the 2002 ECMWF fields. The estimated accuracy of the fit is for almost all latitude bands an upper limit, except for the high latitudes on the Northern Hemisphere albeit that the values are close. In the equatorial region the estimated standard deviation of the Bayesian fit is larger than the variance of 2002 different fits and 2002 ECMWF fields. This is caused by the fact that the magnitude of the estimated error is related to

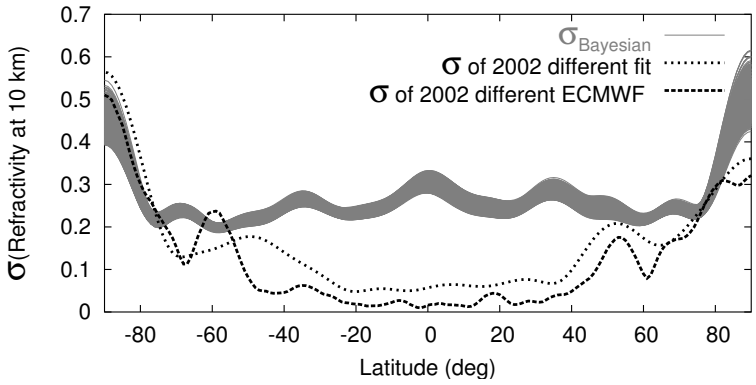

Figure 4.10: Zonal fit error estimate of refractivity at $10km$ for 2002 different fits (grey) lines, the standard deviation of the 2002 zonal fits and the standard deviation of the 2002 zonal mean ECMWF fields. The 2002 data sets are constructed by excluding 5 days out of a 14 day period.

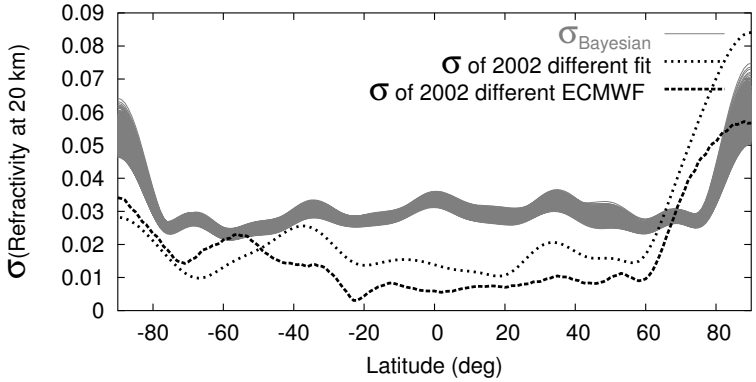

Figure 4.11: Analogue to Figure 4.10 except here refractivity at $20km$ is used.

the density of observation. In the equatorial region, however, the atmospheric variability is small and thus the standard deviation of 2002 different fits or ECMWF fields will be small as well.

5. Results

In this chapter results of the fitting are shown. Besides the 18 month of CHAMP data, ECMWF fields are used to determine the expected accuracy when global maps based on METOP observations are constructed. These (simulated) observations are obtained using analysis fields from ECMWF 6 hour analysis.

First monthly global fields of refractivity at certain heights are constructed and the accuracy is discussed. Next zonal mean of geopotential, refractivity and temperature are determined and compared to ECMWF zonal mean values. The last section presents the zonal mean geopotential height thickness and some related aspects.

Monthly Global Fields

Refractivity

Using (simulated) METOP observations monthly global fits are made using bayesian fitting. Recall that refractivity versus height is closely related to observed quantity by GPS-RO techniques. The relationship requires some assumptions although not many (see Chapter 2 and Rubek (2004)). The

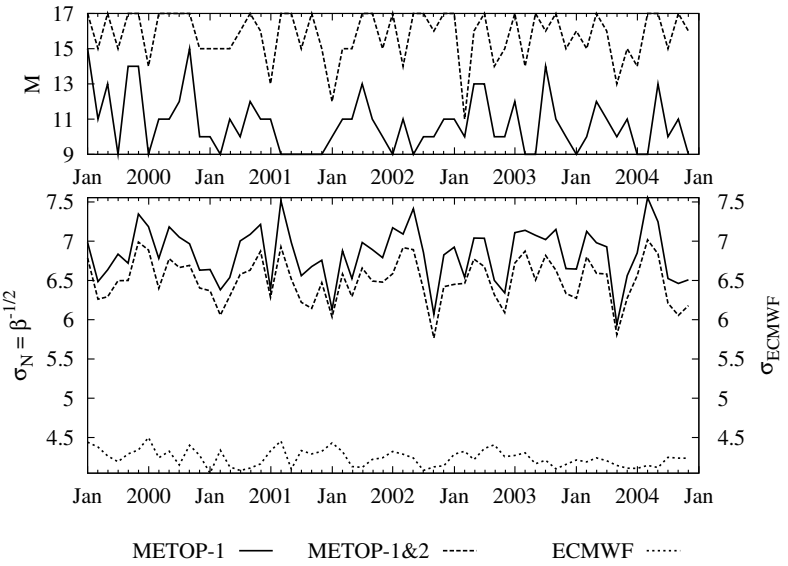

Figure 5.1: Results of bayesian fitting of monthly data over a period of 5 years. Observations of refractivity at a height of 5km are obtained from ECMWF analysis fields with based on one (solid line) and two (dashed line) space-borne METOP. The top panel shows the optimal number of spherical harmonics; the bottom panel shows the estimated accuracy together with the global monthly standard deviation from ECMWF analysis fields.

observed parameter is refractivity at a certain height over a 5 year period. Furthermore, a second dataset is constructed by simulating two GRAS receivers in space. Comparing these two datasets gives some insight in the future accuracy of global maps retrieved from GPS-RO.

Figure 5.1 shows the optimal number of spherical harmonics and the estimated accuracy for monthly global maps of refractivity at a height of 5 km. For a single GRAS receiver the optimal number of spherical harmonics varies between 9 and 14 (Figure 5.1 top panel). There does not really seem to be a seasonal relationship with respect to the number of spherical harmonics. The optimal number of spherical harmonics using two GRAS receivers increases; ranges between 12 and 17 are observed. In the bottom panel the estimated accuracy is presented together with the global monthly standard deviation of the ECMWF refractivity at 5 km. Clearly, the estimated accuracy overestimates the ECMWF standard deviation. This is due to the fact that the number of observations per day is approximately 500 for METOP-1 (1000 for METOP-1&2), which sets an upperbound of the number of spherical harmonics that can be used for the fit. The estimated accuracy is related to the result of the fitting resolution an decreases towards the actual value (see Figure 4.9); the optimal value is $M \approx 11$ and $M \approx 15$ for METOP-1 and METOP-1&2 respectively which is apparently too small for the monthly global mean of refractivity at 5km.

In Figure 5.2 the optimal number of spherical harmonics and estimated accuracy is shown for a refractivity at a height of 8 km. The number of optimal harmonics lies between 9 and 11 and between 10 and 13 for METOP-1 and METOP-1&2 data respectively. The estimate standard deviation attains a maximum at February-March. The same yields for the monthly standard deviation as observed by ECMWF analysis. The estimated accuracy (METOP-1 and METOP-1&2) and the observed accuracy (ECMWF) are very close: the number of spherical harmonics is high enough to estimate monthly refractivity at 8 km fields with a similar accuracy as the truth (i.e. ECMWF analysis fields). Figure 5.3 shows a similar figure as the previous figures only now for refractivity at 10 km. The optimal number of spherical harmonics is a little smaller than for 8km but the estimated and the actual error (or standard deviation) are very close.

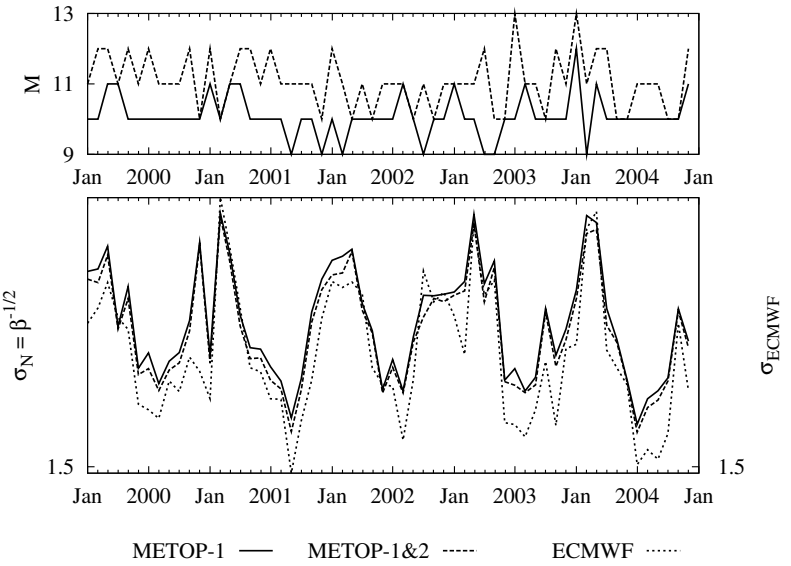

Figure 5.2: Similar to Figure 5.1 except here refractivity at 8km is used.

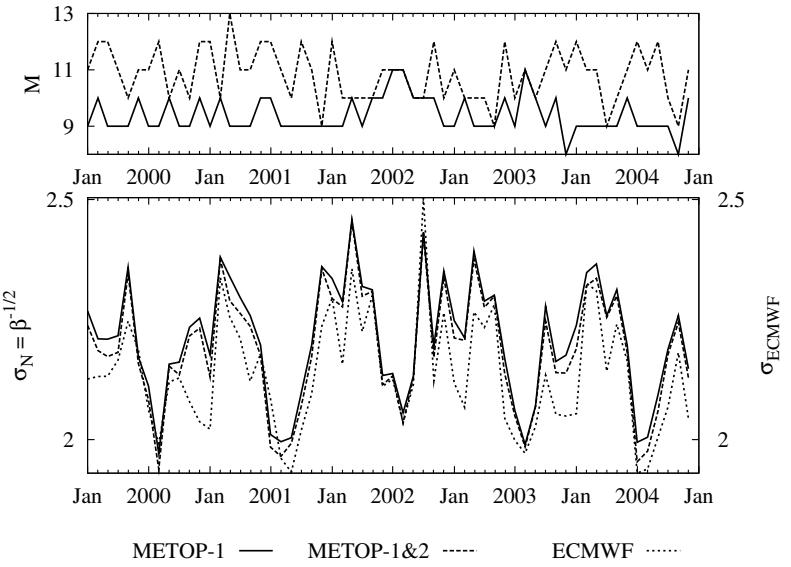

Figure 5.3: Similar to Figure 5.1 except here refractivity at 10km is used.

The above error estimates where obtained using simulated observations, that is the observations where retrieved from the ECMWF analysis. For a six month period the monthly global mean refractivity at 10 kilometer height is determined using real and simulated CHAMP data. The estimated error is shown in Figure 5.4 together with the monthly variability of ECMWF. The estimated error obtained using simulated observations lies again close to the atmospheric variability. The estimated error of real CHAMP data is approximately 0.2 larger than the estimated error from simulated data and the offset seems constant. The two data sets (CHAMP and simulated CHAMP) have the same coverage and thus the difference stems from the difference in observed values and can be regarded as the observation error. The magnitude of this error is not simply the difference between the estimated errors because the estimated error is relative to the fitting which is not perfect.

Geopotential Height

The global mean geopotential height as constructed using CHAMP data for the month May 2003 is shown in Figure 5.5(a). A total of 4373 observations are used to fit a spherical harmonic

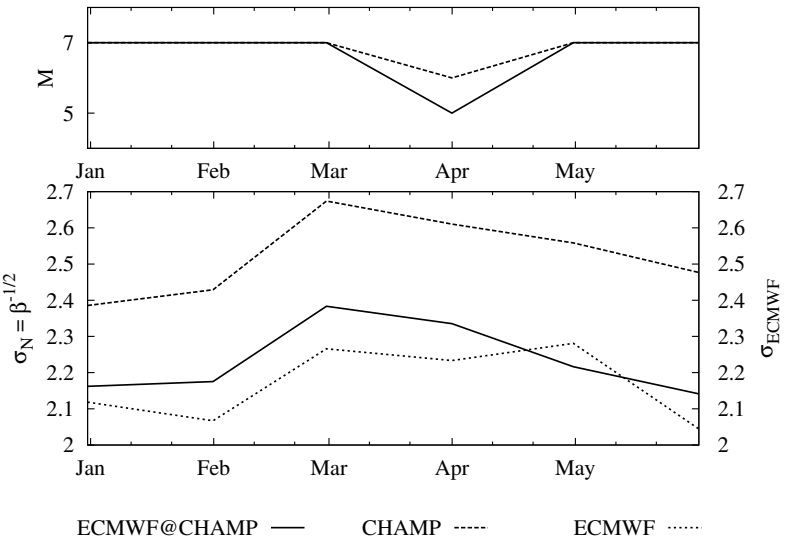

Figure 5.4: Results of Bayesian fitting using real and simulated CHAMP data. Mean monthly global 10 kilometer refractivity fields are determined. The top panel shows the optimal number of spherical harmonics for CHAMP (dashed) and simulated CHAMP (solid); the bottom panel shows the monthly standard deviation of ECMWF analysis (dotted) and the estimated standard deviation of CHAMP and simulated CHAMP Bayesian fits.

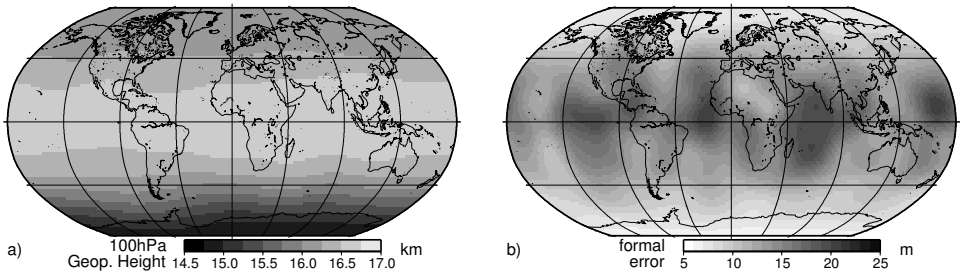

Figure 5.5: a) Global mean 100hPa geopotential height field valid for May 2003 based upon CHAMP data; b) Global formal error field.

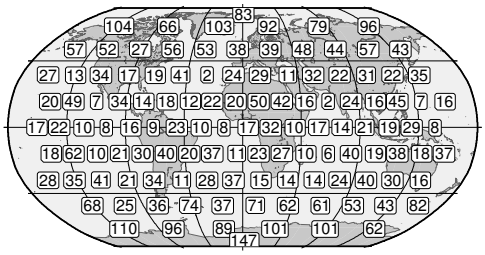

Figure 5.6: Number of CHAMP observation for the month May 2003 as observed in 120 equal areas.

representation using 7 harmonics. Figure 5.5(b) shows the formal error of the fit which is related to the coverage and quality of the observations. The formal error attains a local maxima around the equator. These maxima are related to data sparse areas. At the poles the formal error has its minimum: around these regions CHAMP observation dense. In Figure 5.6 the number of CHAMP observations over the globe are shown. The data sparse region are clearly visible in the plot of the formal error.

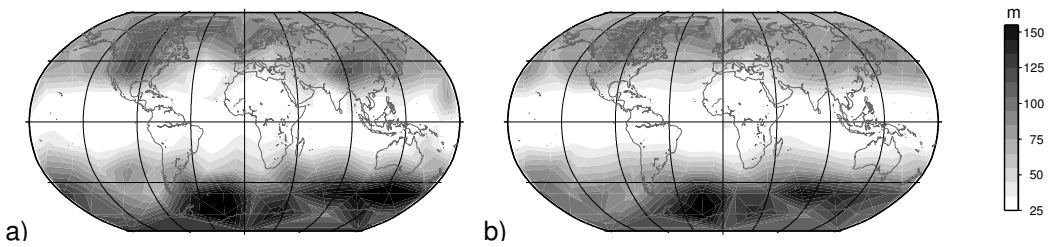

Figure 5.7: a) Standard deviation of CHAMP observation minus fit for May 2003; b) Atmospheric variation of ECMWF analysis for May 2003. The statistics are determined using a partitioning of the globe into 120 areas.

Figure 5.7(a) shows the variation of the CHAMP observations minus the fit. The atmospheric variation is shown in Figure 5.7(b). In order to make a sensible comparison, the statistics of both global fields are constructed using a partitioning of the globe in to 120 (almost) equal areas (see Section 3.4). The variation is small around the equator in both cases. This is due to the fact that the geopotential height does not vary much during the month May around the equator. Both maps show a large similarity: the maxima above North America and Scandinavia, around 45^{o}W and 60^{o}E in the in southern polar region. The magnitude of the maxima of the CHAMP observations is a little larger than the maxima of the atmospheric variation. Part of this difference may be related to observation noise but, especially for the southern maxima, the atmospheric variation in the model may also differ from reality. There are two regions with high variability in CHAMP data which are not present in the ECMWF field: the region near the Himalaya mountains and the region right below Australia. The first offset may be due to the high mountains: the resolution of the ECMWF orography may be to coarse with respect to the observation resolution of CHAMP data. Another cause might be that the used geoid model to determine the geopotential height fails in this region. The second region (below Australia) is right over the ocean and cannot be explained by orographic effects.

Zonal Mean Fields

The zonal mean geopotential height at 100hPa is shown Figure 5.8(a) obtained from ECMWF analysis for a period of 5 years. The maximum lies around the equator during the whole year. This maximum moves with the Inter Tropical Convergence Zone. The range of 100hPa geopotential height is between 14.5 and 17 km. The minimum values are achieved in the antarctic winter; the atmosphere in antarctic winter is thinner than in artic winter. Figure 5.8(b) shows the temperature at 100hPa. Figure 5.8(c) shows the refractivity at 100hPa. Note that the color scale is inverted such that regions with in both Figure Figure 5.8(a) and (b) the antarctic summer regions are dark shaded. The mean geopotential height in the northern higher latitudes over 5 years is higher than this mean at the southern counter part of the hemisphere. The refractivity and temperature are inversely correlated due to the definition of refractivity: compare Figure 5.8(b) and 5.8(c). Note also that the temperature (and thus the refractivity as well) shows an anomaly in mid September 2002 near the south pole.

In Figure 5.9 zonal fit of CHAMP data for the same parameters are presented. The zonal fits are constructed using data sets of one week. The graphs are very similar to those obtained from ECMWF. Moreover the anomaly observed in mid September near the south pole is also present in the CHAMP temperature and refractivity zonal mean.

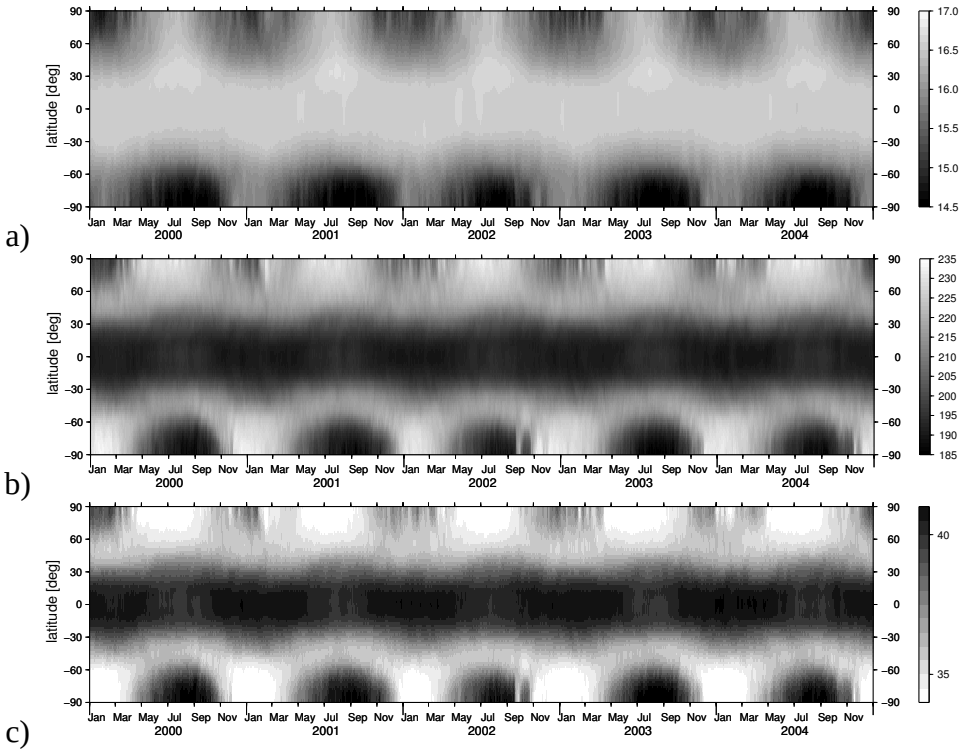

Figure 5.8: Zonal mean of ECMWF fields at 100hPa from 2000 to 2005: a)geopotential height, b) temperature and c) refractivity.

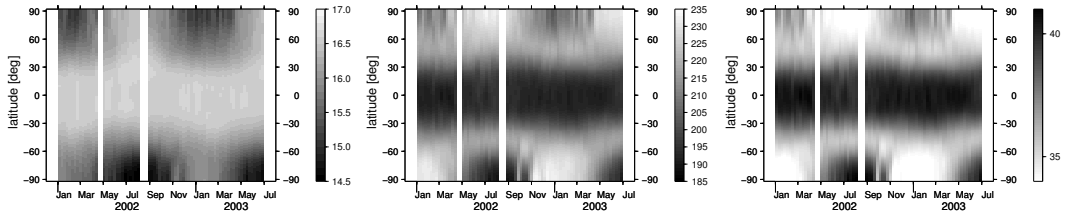

a) b) c)

Figure 5.9: Zonal mean based on fit of CHAMP data 100hPa from January 2002 to July 2003: a)geopotential height, b) temperature and c) refractivity.

Zonal Mean Geopotential Thickness

The zonal mean of the geopotential height difference is obtained from ECMWF analysis fields and from CHAMP radio-occultation observations. A zonal bayesian fit is applied to the CHAMP data and a data window of 7 days is used for each estimate.

In Figure 5.10 the zonal mean of three latitude bands are shown (latitude equal to +50 0 and -50 from top to bottom). For the latitude bands -50 and +50 the CHAMP estimate matches the ECMWF analysis very good apart from the period a period in early 2002 (See Section 2.2.1). For the equatorial band the level thickness as obtained using CHAMP data is underestimated. This is due to the fact that the method to calculate this thickness assumes that the atmosphere is dry. In the tropics, this will not be the case which implies that the used conversion

$$T = k_1 \frac{p}{N} \tag{5.1}$$

does not hold at 400hPa. When plotting the geopotential height difference for the levels 100-300hPa and 100-400hPa for the equator, this effect is clearly visible, see Figure 5.11. In this figure the

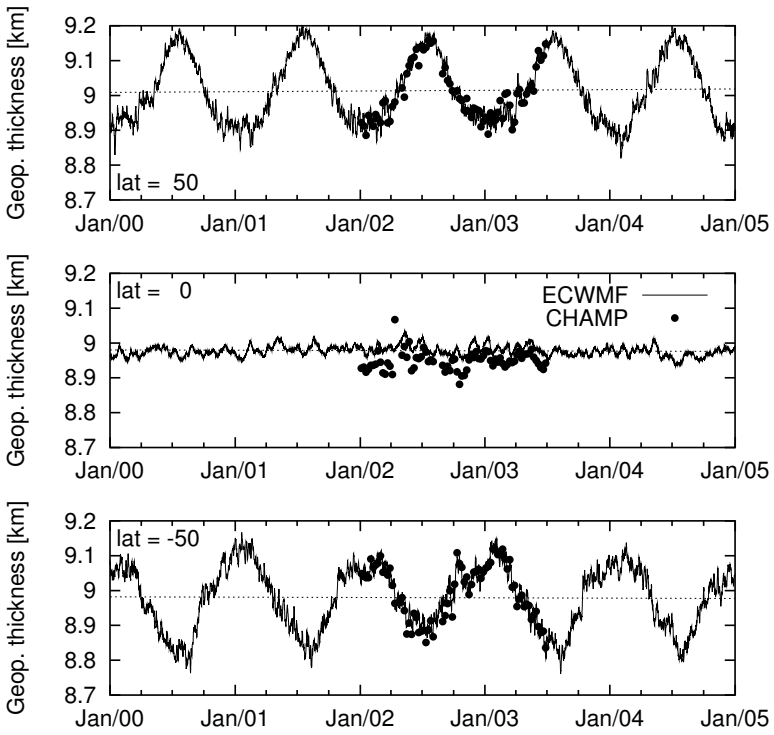

Figure 5.10: Zonal mean geopotential thickness of the layer between 400 and 100hPa for three different latitude bands: 50 degrees (top panel), equator (middle panel) and -50 degrees (bottom panel). The solid line is the ECMWF geopotential thickness; the dots are 7 day zonal fits of CHAMP data and the solid line is the linear fit of the ECMWF data.

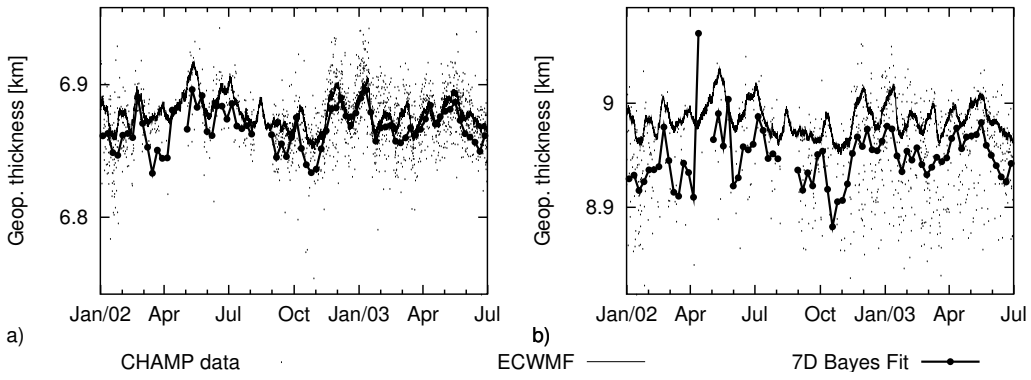

Figure 5.11: Geopotential height thickness at the equator for a) between 100 and 300hPa, b) between 100 and 400hPa. ECMWF is denoted by the solid line; dots are CHAMP data and lines with dots is the 7 day zonal fit.

CHAMP zonal fit is presented together with the observations and the ECMWF fit for the geopotential thickness. Observed layer thickness by CHAMP of 100-300hPa is very similar to the corresponding ECMWF layer thickness. The layer thickness of the 100-400hPa as obtained using CHAMP data shows to have an offset, while the change in time is more or less the same as the the layer thickness of ECMWF.

6. Conclusions

In this study the use of space borne Global Positioning System Radio Occultation (GPS-RO) data to estimate global maps is investigated. The global maps are constructed using Bayesian fitting.

Assumptions have to be made as with all methods which ingest data into a model to reconstruct a field. The main assumption for Bayesian fitting is the choice of the type of basis functions. Here spherical harmonics representation is used, a type of function widely used for describing fields on a sphere (i.e the earth).

Bayesian fitting is just an extention of least squares fitting with the extension being a decision mechanism for finding the optimal number of basis function. The method of fitting data is chosen above other methods (such as Kriging and assimilation) because for this technique no observation error correlations or background error correlations are needed. Fitting, using a time window, immediately creates an average value map and, as long as the observation are regular in time and space, this map will represent the actual mean.

Another advantage of the Bayesian fitting method is that an estimate of the observation error is obtained. Although this estimate is pure related to the fit itself it is a valuable parameter associated with the data set used and may reveals problems with the data.

The method of observation is based on a time delay measurement which makes GPS-RO inherently calibration free. This fact is very profitable for climate research. The GPS-RO observable is (in the end) refractivity and all other parameters (dry temperature and pressure) are derived and require extra assumptions.

The real data used in this study was measured by CHAMP and was processed by DMI according to the proposed processing scheme for the GRAS-SAF. To inspect the future data set of GPS radio occultation, METOP observations are simulated by extracting the parameters temperature, geopotential height and refractivity from ECMWF analysis fields.

The current data set of CHAMP data is not large enough with respect to coverage to create monthly mean fields with large enough spherical harmonics. Due to the height of the orbit (approximately 300 km) the observations are mainly in the high latitudes. Moreover, the daily repetition due to this low orbit is restricted to small bands in the longitude implying that the diurnal cycle of the observed parameter is not well sampled. At the other hand, the data volume and coverage (both spatial and temporal) is good enough to estimate zonal means.

METOP will fly in a higher orbit and thus will have more observation around the equator although this coverage will still be biased towards the mid latitudes. A single METOP receiver will also show a daily repetition in longitude bands but these bands are much broader than for CHAMP due to the difference in orbit height. However, two METOP satellites with a GRAS receiver in different orbits will sample the diurnal cycle adequately. Data from a single METOP receiver is sufficient for estimating global fields at heights of 8 km ($\approx$ 350 hPa) and higher.

The Bayesian fitting method has proven to be valuable for estimating (1) zonal means of, for example, geopotential height (CHAMP) and (2) global fields of, for example, refractivity at 10 km (METOP). When the fit is good the estimated error lies very close to the standard deviation of the parameter within one month. GPS-RO data, given that the coverage and the daily sample rate is good, is an independent source of information with which global maps can be constructed. The future space based GPS receivers will definitely contribute as an independent global climate monitoring system.

Acknowledgments

The author would like to thank the GRAS-SAF team for their hospitality and helpful discussions. Special thanks are addressed to Georg Larsen, Kent Lauritsen, Franz Rubek and Martin Sörensen who provided all the relevant documentation, data and infrastructure. Martin Stendl and Henrik Vedel are thanked their input and discussion. EUMETSAT and SRON (National Institute for Space Research, the Netherlands) are thanked for funding this project. GFZ kindly provided the data used in this study.

References

Bevis, M., and S. Businger, and T.A. Herring, and C. Rocken, and R.A. Anthes, and R.H. Ware, 1992: GPS meteorology: Sensing of atmospheric water vapor using the global positioning system, *J. Geophys. Res.*, **97**, 15787–15801.

Born, M., and E. Wolf, 1980: *Principles of Optics*, Pergamon Press.

ECMWF, 1995: MARS User Guide B6.7/2, *Computer Bulletin*, European Centre for Medium-Range Weather Forecasts.

Fjeldbo, G., and J. Kliore, and V. Eshleman, 1971: The neutral atmosphere of venus as studied with the mariner v radio occultation experiments, *The Astronomical Journal*, **76**, 123–140.

Galassi, M., and J. Davies, and J. Theiler, and B. Gough, and G. Jungman, and M. Booth, and F. Rossi, 2003: *GNU Scientific Library Reference Manual - 2nd Edition*, Network Theory Limited, 601 pp, ISBN 0-9541617-3-4.

Gobiet, A., and U. Foelsche, and A.K. Steiner, and M. Borsche, and G. Kirchengast, and J. Wickert, 2005: Climatological validation of stratospheric temperatures in ECMWF operational analyses with CHAMP radio occultation data, *Geophys. Res. Lett.*

Hedin, A. E., 1991: Extension of the MSIS thermosphere model into the middle and lower atmosphere, *J. Geophys. Res.*, **96**, 1159–1172.

Hocke, K., and G. Kirchengast, and A.K. Steiner, 1997: Ionospheric correction and inversion of GNSS occultation data: Problems and solutions, *Technical report no. 2*, ESA/ESTEC IMG/UoG.

Hofmann-Wellenhof, B., and H. Lichtenegger, and J. Collins, 1992: *Global Positioning System theory and practice*, Springer-Verlag, 355 pp.

Kursinski, E. R., and G. A. Hajj, and W. I. Bertiger, and S. S. Leroy, and T. K. Meehan, and L. J. Romans, and J. T. Schofield, and D. J. McCleese, and W. G. Melbourne, and C. L. Thornton, and T. P. Yunck, and J. R. Eyre, and R. N. Nagatani, 1996: Initial results of radio occultation observations of earth's atmosphere using the global positioning system, *Science*, **271**, 1107–1110.

Kursinski, E.R., and G.A. Hajj, and J.T. Schofield, and R.P. Linfield, and K.R. Hardy, 1997: Observing earths atmosphere with radio occultation measurements using the global positioning system, *J. Geophys. Res.*, **102**, 23429–23465.

Laprise, R., 1992: The resolution of global spectral models, *Bull. Amer. Meteor. Soc.*, **73**, 1453–1454.

Leiterer, U., and H. Dier, and T. Naebert, 1997: Improvements in radiosonde humidity profiles using RS80/RS90 radiosondes of vaisala, *Beitr. Phys. Atmosph.*, **124**, 319–336.

Lemoine, F. G., and S. C. Kenyon, and J. K. Factor, and R. G. Trimmer, and N. K. Pavlis, and D. S. Chinn, and C. M. Cox, and S. M. Klosko, and S. B. Luthcke, and M. H. Torrence, and Y. M Wang, and R. G. Williamson, and E. C. Pavlis, and R. H. Rapp, and T. R. Olson, 1998: The development of the joint NASA GSFC and the NIMA geopotential model EGM96, *NASA TP/-1998-206861*, NASA Goddard Space Flight Center.

Leroy, S. S., 1997: Measurement of geopotential heights by GPS radio occultation, *J. Geophys. Res.*, **102**, 6971–6986.

Lorenc, A.C., and D. Barker, and R.S. Bell, and B. Macpherson, and A.J. Maycock, 1996: On the use of radiosonde humidity observations in mid-latitude NWP, *Meteor. Atmos. Phys.*, **60**, 3–17.

MacKay, D. J. C., 1992: Bayesian interpolation, *Neur. Comp.*, **4**, 415–447.

Marouf, E. A., and G. Tyler G, and P. Rosen, 1986: Profiling saturn's rings by radio occultation, *Icarus*, **68**, 120–166.

Melbourne, W. G., and E. S. Davis, and C. B. Duncan, and G. A. Hajj, and K. R. Hardy, and E. R. Kursinski, and T. K. Meehan, and L. E. Young, and T. P. Yunck, 1994: The application of spaceborne gps to atmospheric limb sounding and global change monitoring, *Jpl publication 94-18*, Jet Propulsion Laboratory.

Rodgers, C. D., 1976: Retrieval of atmospheric temperature and composition from the remote measurement of radiation, *Reviews of Geophysics and Space Physics*, **14**, 609–624.

Rubek, F., 2004: GRAS meteorology SAF science plan, *SAF/GRAS/DMI/ALG/SP/001, version 3.1*, Danmarks Meteorologiske Institut.

Wallace, J. M., and K-H. Lau, and Y. Zhang, 1993: Structure and seasonality of interannual and interdecadal variability of the geopotential height and temperature fields in the northern hemisphere troposphere, *J. Climate*, **6**, 2063–2082.

Wickert, J., and C. Reigber, and G. Beyerle, and R. Koenig, and C. Marquardt, and T. Schmidt, and L. Grunwaldt, and R. Galas, and T. K. Meehan, and W. G. Melbourne, and K. Hocke, 2001: Atmosphere sounding by GPS radio occultation: First results from CHAMP, *Geophys. Res. Lett.*, **28**, 3263–3266.

A. Spherical Harmonics Definition

There are a number of different definitions of spherical harmonics. Here the definition of used in the ECMWF model is used (ECMWF (1995)). A field $X(\lambda, \mu)$ is represented by

$$X(\lambda,\mu) = \sum_{m=-M..M} \sum_{n=|m|..M} X_n^m e^{im\lambda} P_n^m(\mu), \tag{A.1}$$

where $P_n^m(\mu)$ are associated Legendre Polynomials of the first kind,

$$\lambda = \text{longitude} \tag{A.2}$$
$$\mu = \sin(\text{latitude}) \tag{A.3}$$

and X_n^{-m} = complex conjugate X_n^m. The number of coefficients is $(M+1)^2$ for real valued fields. m is called the order and n is called the degree of the spherical harmonic. Another way of writing the

spectral harmonics representation is

$$X(\lambda,\mu) = \sum_{n=0..M} a_n^0 P_n^0(\mu) \quad (A.4)$$

$$+ \sum_{m=0..M} \sum_{n=m..M} (a_n^m cos(m\lambda) + b_n^m sin(m\lambda)) P_n^m(\mu), \quad (A.5)$$

where

$$a_n^m = \frac{1}{2}(Re(X_n^m) + Re(X_n^{-m})) \text{ for } m = 0..M, n = m..M \quad (A.6)$$

$$b_n^m = \frac{1}{2}(Im(X_n^m) - Im(X_n^{-m})) \text{ for } m = 0..M, n = m..M \quad (A.7)$$

One caution should be made here. The fitting method may become ill-posed when an observation lies very close to one of the poles. These observations are therefore excluded from the data set.

The associated Legendre polynomials of the first kind are defined as (for $m = 0..M$)

$$P_m^m(\mu) = \prod_{k=1}^{m-1} \sqrt{\frac{2(k+1)+3}{2(k+1)}} (1-\mu^2)^{(m-k+1)/2} \quad (A.8)$$

$$P_{m+1}^m(\mu) = \prod_{k=1}^{m-1} \sqrt{\frac{2(k+1)+3}{2(k+1)}} \sqrt{2m+1} (1-\mu^2)^{(m-k+1)/2} \mu \quad (A.9)$$

$$P_n^m(\mu) = \sqrt{\frac{4(n-1)^2-1}{(n-1)^2-m^2}} \left(\mu P_{n-1}^m(\mu) - \sqrt{\frac{4n^2-1}{n^2-m^2}} P_{n-2}^m(\mu) \right) \quad (A.10)$$

for $n = m+2 \ldots M$

Another way of writing the associated polynomials is by

$$P_n^m(\mu) = \sqrt{(2n+1)\frac{(n-m)!}{(n+m)!}} \frac{1}{2^n n!} (1-\mu^2)^{m/2} \frac{d^{n+m}}{d\mu^{n+m}} (\mu^2-1)^n, \quad (A.11)$$

for $m \geq 0$ and $P_n^{-m}(\mu) = P_n^m(\mu)$.

B. Formal Error Estimates

Least squares fit

Recall that the least squares fit is defined by

$$\min_w (y - \Phi w)^T (y - \Phi w), \quad (B.1)$$

where

$$\Phi = \{\phi_k(x_i)\sigma_i^{-1}\} \text{ and } y = \{y_i \sigma^{-1}\}, \quad (B.2)$$

where σ_i are known errors. The solution of Equation is B.1 is

$$w = (\Phi^T \Phi)^{-1} \Phi^T y, \quad (B.3)$$

The equation for the j-th coefficient is

$$w_j = \sum_{i=1}^{N} \sum_{k=1}^{M} (\Phi^T \Phi)_{jk}^{-1} \frac{\phi_k(x_i)}{\sigma_i} \frac{y_i}{\sigma_i} \quad (B.4)$$

An estimate of the formal error of the coefficients can be obtained by

$$\sigma^2(w_j) = \sum_i^N \sigma_i^2 \left(\frac{\partial w_j}{\partial y_i}\right)^2 \tag{B.5}$$

$$= \sum_{k=1}^M \sum_{m=1}^M (\Phi^T\Phi)^{-1}_{jk} (\Phi^T\Phi)^{-1}_{jm} \sum_{i=1}^N \frac{\phi_m(x_i)}{\sigma_i} \frac{\phi_k(x_i)}{\sigma_i} \tag{B.6}$$

$$= \sum_{k=1}^M \sum_{m=1}^M (\Phi^T\Phi)^{-1}_{jk} (\Phi^T\Phi)^{-1}_{jm} (\Phi^T\Phi)_{km} = (\Phi^T\Phi)^{-1}_{jj} \tag{B.7}$$

When the errors σ_i are not known one can assume that all errors are equal, that is $\sigma = \sigma_i$. This leads to a different function to minimize: q

$$\chi^2(w) = (y' - \Phi' w)^T (y' - \Phi' w), \tag{B.8}$$

where Φ' and y' are defined as

$$\Phi' = \{\phi_k(x_i)\} \text{ and } y' = \{y_i\}, \tag{B.9}$$

The solution to this equation is similar to Equation B.3 and an estimate of the coefficient accuracy becomes

$$\sigma^2(w_j) = \sigma^2 \sum_i^N \left(\frac{\partial w_j}{\partial y_i}\right)^2 \tag{B.10}$$

$$= \sigma^2 (\Phi'^T \Phi')^{-1}_{jj}, \tag{B.11}$$

where σ can be estimated by

$$\sigma^2 = \frac{\chi^2(w)}{N - M}, \tag{B.12}$$

with χ^2 obtained from Equation B.8.

Bayesian fit

The solution for of the bayesian minimization function

$$M(w, \alpha, \beta) = \frac{1}{2}\alpha\, w^T C w + \frac{1}{2}\beta (y - \Phi w)^T (y - \Phi w), \tag{B.13}$$

where Φ and y are defined as

$$\Phi = \{\phi_k(x_i)\} \text{ and } y = \{y_i\}, \tag{B.14}$$

is given by

$$w_j = \beta \sum_{i=1}^N \sum_{m=1}^M A^{-1}_{jm} \phi_m(x_i) y_i, \tag{B.15}$$

where $A = \alpha C + \beta \Phi^T \Phi$. An estimate of the coefficient accuracy becomes

$$\sigma^2(w_j) = \sigma^2 \sum_i^N \left(\frac{\partial w_j}{\partial y_i}\right)^2 \tag{B.16}$$

$$= \sigma^2 \beta^2 \sum_{k=1}^M \sum_{m=1}^M A^{-1}_{jk} A^{-1}_{jm} (\Phi^T\Phi)_{km}, \tag{B.17}$$

where σ can be estimated by

$$\sigma^2 = \frac{(y - \Phi w)^T (y - \Phi w)}{N - M}. \tag{B.18}$$

An estimate of σ^2 is $1/\beta$.

C. Properties of the Evidence Maximum

The maximum of the logarithm of the evidence defined by

$$\begin{aligned} \log(E) &= -\alpha E_w(w_{mp}) - \beta E_d(w_{mp}) \\ &\quad -\frac{1}{2}\log\det A + \frac{1}{2}M\log\alpha + \frac{1}{2}N\log\beta - \frac{1}{2}N\log 2\pi \end{aligned} \tag{C.1}$$

should satisfy the requirements that the derivatives to α and β are both zero, that is

$$0 = -E_w(w_{mp}) - \frac{1}{2}\,\text{Trace}\left(A^{-1}C\right) - \frac{1}{2}\,M\,\alpha^{-1} \tag{C.2}$$

$$0 = -E_d(w_{mp}) - \frac{1}{2}\,\text{Trace}\left(A^{-1}B\right) - \frac{1}{2}\,N\,\beta^{-1}, \tag{C.3}$$

where $B = \Phi^T\Phi$. Rewriting these equations gives

$$2\alpha E_w(w_{mp}) = M - \alpha\,\text{Trace}\left(A^{-1}C\right) \tag{C.4}$$

$$2\beta E_d(w_{mp}) = N - \beta\,\text{Trace}\left(A^{-1}B\right) \tag{C.5}$$

The trace of a matrix is equal to the sum of the eigenvalues. The eigenvalues of on inverse matrix are the reciproques of the matrix. Furthermore $(A^{-1}C)^{-1} = C^{-1}A = \alpha I + \beta C^{-1}B$. Assume that the eigenvalues of $C^{-1}B$ are λ_i than the trace of $A^{-1}C$ becomes

$$\text{Trace}\left(A^{-1}C\right) = \sum_{i=1}^{M}\frac{1}{\alpha + \beta\lambda_i} \tag{C.6}$$

The trace of $A^{-1}B$ is calculated using $B^{-1}A = \alpha B^{-1}C + \beta I$, and is

$$\text{Trace}\left(A^{-1}B\right) = \sum_{i=1}^{M}\left(\frac{\alpha}{\lambda_i} + \beta\right)^{-1} = \sum_{i=1}^{M}\frac{\alpha}{\alpha + \beta\lambda_i} \tag{C.7}$$

The relation between the last two equations is

$$\beta\,\text{Trace}\left(A^{-1}B\right) = M - \alpha\,\text{Trace}\left(A^{-1}C\right) \tag{C.8}$$

Introducing a new variable γ results in the following equations for the optimal evidence

$$\begin{aligned} \gamma &= M - \alpha\,\text{Trace}\left(A^{-1}C\right) \\ 2\alpha E_w(w_{mp}) &= \gamma \\ 2\beta E_d(w_{mp}) &= N - \gamma \end{aligned} \tag{C.9}$$

The meaning of γ can be seen as the number of good parameter measurements. Iteratively a solution to Equation C.9 can be found.